Effects of surfactant transport on electrodeformation of a viscous drop

Herve Nganguia
Department of Mathematical and Computer Sciences, Indiana University of Pennsylvania, Indiana, Pennsylvania 15705, USA

On Shun Pak
Department of Mechanical Engineering, Santa Clara University, Santa Clara, California 95053, USA

Y.-N. Young*
Department of Mathematical Sciences, New Jersey Institute of Technology, Newark, New Jersey 07102, USA

(Received 13 November 2018; revised manuscript received 26 April 2019; published 10 June 2019)

In this work we quantify the effects of surfactant transport on the deformation of a viscous drop under a DC electric field. We study how convective and diffusive transport of surfactants at drop surfaces influence the equilibrium and dynamic deformation of a leaky dielectric drop and a conducting drop. Focusing on the prolate drop shape (elongates along the electric field), we show the differences in equilibrium deformation and flow circulation between a leaky dielectric drop and a conducting drop. We quantify the drop electrodeformation via its dependence on the interior flow circulation and the dominant surfactant transport regime (characterized by the surface Péclet number Pe_s). For a leaky dielectric drop with dominant surfactant diffusion ($\mathrm{Pe}_s \ll 1$), equator-to-pole (pole-to-equator) circulation yields smaller (larger) equilibrium deformation with increasing surfactant coverage, compared to a clean drop. However, when convection dominates ($\mathrm{Pe}_s \gg 1$), the equilibrium drop deformation increases (decreases) with larger surfactant coverage for equator-to-pole (pole-to-equator) circulation. Larger equilibrium drop deformation is found for a leaky dielectric drop than a conducting drop when the interior flow is from equator to pole. For an interior flow from pole to equator, we identify cases where larger deformation is found for a conducting interior fluid. Finally, we study the effect of the surfactant transport on the dynamic evolution of drop shape. We found the drop undergoes an overshoot in the early deformation phase, before settling to its equilibrium shape—similar to the overshoot observed for unsteady Stokes flow.

DOI: 10.1103/PhysRevE.99.063104

I. INTRODUCTION

Electric field is widely utilized to deform a viscous drop in microfluidics and many petroleum engineering applications. For a leaky dielectric drop freely suspended in another leaky dielectric fluid, the bulk charge neutralizes on a fast timescale while free charges accumulate on the drop surface under an electric field. Analytical investigation of the electrodeformation of a viscous drop has been conducted [1,2], and the electrohydrodynamic (EHD) leaky dielectric model [3] has been developed to explain the deformation of conducting drops suspended in a conducting medium. Results show that the electrostatic stresses on the drop surface lead to interior toroidal circulations. Consequently, the drop deforms to either a prolate or an oblate spheroid shape depending on the specific electrical properties of fluids [4]. With different electrical properties the effects of the electrostatic and hydrodynamic stresses on drop deformation also behaves distinctively [5]. Under a small electric field, a steady equilibrium drop shape exists due to the balance between the electric and hydrodynamic stresses [6–8]. Under a sufficiently large electric field, no steady equilibrium drop shape is stable and the drop keeps deforming until the eventual break-up into smaller drops [9,10].

Analytical treatments of the electrodeformation in the leaky dielectric framework assume either small deformations or specific spheroidal (oblate or prolate) shapes. These results predict the dependence of the equilibrium drop shape on the electric capillary number (ratio of electric stress to surface tension). Such dependence was first derived by Taylor [3] for small deformation of a spherical drop in a weak uniform electric field. A comprehensive review of the theoretical developments in this area can be found in Melcher and Taylor [4] and Saville [5]. Bentenitis and Krause [11] extended Taylor's leaky dielectric model for large deformation of a noncharged viscous drop in a dielectric fluid by a strong electric field. Their large deformation analysis assumes spheroidal shapes and gives reasonable agreement with most experiments for the prolate drops, while discrepancies are observed for oblate drops. Zabarankin reformulated the stress boundary condition on a spheroidal drop and used a non-Stokes stream function to calculate the steady flow around a spheroidal drop under a DC electric field [12,13]. In this new formulation Zabarankin predicted large steady prolate spheroidal drop deformation consistent with results from both experiments and previous spheroidal models.

Direct numerical simulations of an axisymmetric or two-dimensional drop in an electric field have been conducted to investigate strong electrodeformation in the framework of the leaky dielectric model [8,14–19]. Under strong electric

*yyoung@njit.edu

forces conical points may form at the end of the viscous drop [20], from where small drops may be streaming as a result of the instability (tip streaming). The viscous drop may also undergo large deformation with undulation, and eventually break up into several drops of comparable sizes. While both phenomena require special numerical treatment to capture the topological changes due to the instability, tip streaming requires numerical resolution for the structures and dynamics at the conical points [15,16].

Recent studies have reported the effects of charge relaxation and convection on the dynamics of drop deformation within the leaky dielectric framework [21–23]. In the absence of charge convection, relaxation affects the transient dynamic of the prolate (oblate) drop by causing a short-lived shape transition at the early phase of drop evolution, but it does not alter the equilibrium deformation. However, without relaxation, charge convection gives rise to monotonic deformation dynamics that asymptotes to an equilibrium with shape-dependent differences: Equilibrium deformation is enhanced for a prolate drop [24] and reduced for an oblate drop (completely stabilized for an otherwise unstable oblate drop) [22]. Lanauze *et al.* [21] also considered inertial effects by solving the unsteady Stokes equation. They show inertia leads to an overshoot in the transient evolution of the drop at the later phase of the dynamic prior to reaching equilibrium; this result is consistent with existing numerical simulations [8,25].

Surfactants are extensively used to reduce drop size by lowering surface tension in many engineering applications that involve drop deformation and breakup [26,27]. Surface tension reduction by surfactant can substantially alter interfacial evolution and the flow: A striking example is the surfactant-induced tip streaming of small drops from a thin viscous thread extended from a bubble deformed by an imposed shear or strain [28]. Experiments and analyses show that surfactant has a significant effect on the stability of a viscous jet surrounded by another viscous fluid. Linear stability of a surfactant-laden cylindrical jet shows that surfactant affects the growth rate of disturbances via a combination of reduced surface tension and the immobilizing (surface stiffening) effect of the Marangoni stress.

The equilibrium electrodeformation of a surfactant-laden viscous drop has been investigated experimentally by Ha and Yang [29,30] (small-deformation analysis and experiments), and later numerically by Teigen and Munkejord [31] (axisymmetric numerical simulations) and semianalytically by Nganguia *et al.* [32] (large deformation analysis). While Ha and Yang concluded that surfactant leads to enhanced electrodeformation for a prolate drop, Teigen and Munkejord found that smaller deformation may be caused by surfactant if the surfactant concentration is small, leading to an opposite circulation inside the viscous drop. These phenomena have been captured and explained by an analytical spheroidal model for a surfactant-laden viscous drop in the limit of weak surfactant diffusivity [32].

The Marangoni stress depends on the surfactant transport characterized by the surface Péclet number Pe_s, the ratio of convective to diffusive transport. To our knowledge, studies on the effects of surfactants on the deformation of drops subject to electric fields [31,32] have focused on transport dominated by convection, where $\mathrm{Pe}_s \gg 1$. While these studies have enhanced our understanding of the combined effects of electric fields and surfactants on the electrohydrodynamics of drops, the influence of diffusive surfactant transport on equilibrium deformation, and on the transient evolution of drops remain unexplored. Here we investigate the effects of surfactants on drop electrodeformation from diffusion-dominant to moderate convective transport ($\mathrm{Pe}_s \leqslant 10$). To this end, we present a semianalytical method to simulate drops electrohydrodynamics over a range of surface Péclet numbers.

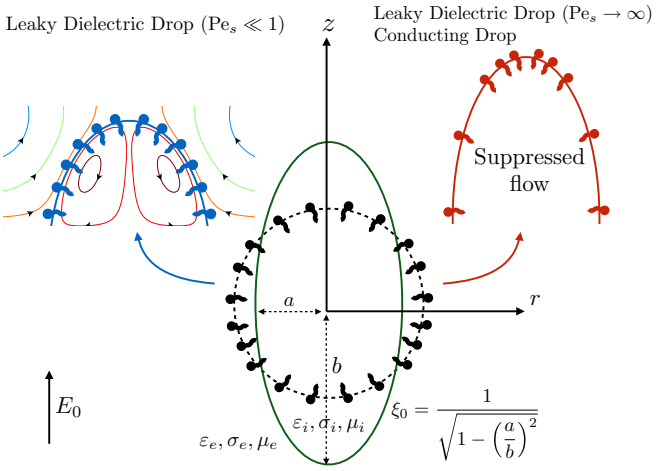

FIG. 1. A viscous drop, subject to a DC electric field $E_0\boldsymbol{e}_z$ and covered with insoluble surfactant (bead-rod particles), separates two immiscible fluids, with physical parameters $\varepsilon_j, \sigma_j, \mu_j$, where $j = i$ denotes the interior of the drop, and $j = e$ its exterior. Application of the electric field induces flow inside and outside the drop, which deforms into a prolate-shaped spheroid at equilibrium. Deformation depends on the type of drops (leaky dielectric or conducting) and on the surfactant transport mechanism (diffusive transport for $\mathrm{Pe}_s \ll 1$ and convective transport for $\mathrm{Pe}_s \to \infty$). The drop shape parameter ξ_0 is a function of the aspect ratio between the major (b) and minor (a) axes.

The paper is organized as follows. In Sec. II we first formulate the leaky dielectric model. We then present the analytical solution in the spheroidal coordinates (Sec. II A 1) and the resulting shape equation for surfactant-laden drops (Sec. II A 2). Finally, we introduce the modified equations for a conducting drop (Sec. II B), before discussing the dependence of surface tension on surfactant concentration in Sec. II C. In Sec. III we validate our spheroidal model against experimental data for a clean conducting drop (Sec. III A) and against numerical simulations for a leaky dielectric, surfactant-laden drop (Sec. III B). We then utilize the model to analyze the effects of surfactant transport on the equilibrium deformation of leaky dielectric and conducting drops (Sec. IV) and on the transient dynamic (Sec. V). Finally, in Sec. VI we draw conclusion on our findings and discuss future research direction.

II. PROBLEM FORMULATION

A. Leaky dielectric drops

We consider a viscous drop immersed in a leaky dielectric fluid as shown in Fig. 1. Each fluid is characterized by the fluid viscosity μ, dielectric permittivity ε, and conductivity σ with the subscript denoting interior (i) or exterior (e) fluid. In this

work the subscript "r" denotes the ratio between exterior and interior quantities: $\mu_r = \mu_e/\mu_i$, $\varepsilon_r = \varepsilon_e/\varepsilon_i$, and $\sigma_r = \sigma_e/\sigma_i$. Typical applications of leaky dielectric fluids involve drops of mm size under an electric field strength of kV/cm. Hence, we can safely assume that the fluid flow in this system is in the creeping flow regime with negligible inertia.

The interior and exterior fluids are governed by the incompressible Stokes equations

$$\mu_j \nabla^2 \boldsymbol{u}_j = \nabla p_j, \tag{1}$$

$$\nabla \cdot \boldsymbol{u}_j = 0, \tag{2}$$

where the subscript j denotes interior ($j = i$) or exterior ($j = e$) fluids. In the far-field the flow is quiescent,

$$\boldsymbol{u}_e(\boldsymbol{x} \to \infty) = \boldsymbol{0}. \tag{3}$$

The drop shape evolves according to

$$\frac{\partial \boldsymbol{X}}{\partial t} = v\boldsymbol{n}, \tag{4}$$

where $\boldsymbol{X}$ is a point on the drop surface and $v = \boldsymbol{u} \cdot \boldsymbol{n}$ is the interfacial velocity along the normal direction $\boldsymbol{n}$.

The stress balance at the drop surface gives

$$[\![(\mathbf{T}^H + \mathbf{T}^E) \cdot \boldsymbol{n}]\!] = \gamma(\nabla \cdot \boldsymbol{n})\boldsymbol{n} - \nabla_s \gamma \cdot \boldsymbol{t}, \tag{5}$$

where $[\![f]\!] \equiv f_e - f_i$ denotes the difference across the drop surface; γ is the surface tension that depends on the surfactant distribution on the surface; $\boldsymbol{t}$ and $\boldsymbol{n}$ are the unit tangential and normal vectors, respectively, on the drop surface; the hydrodynamic stress $\mathbf{T}^H = -p\mathbf{I} + \mu[(\nabla \boldsymbol{u})^T + \nabla \boldsymbol{u}]$, and the Maxwell stress $\mathbf{T}^E = \varepsilon \boldsymbol{E}\boldsymbol{E} - \frac{1}{2}\varepsilon(\boldsymbol{E} \cdot \boldsymbol{E})\mathbf{I}$, with ε the permittivity of the fluid. We can write the Maxwell stress for a leaky dielectric drop in terms of the permittivity and conductivity ratios,

$$[\![\mathbf{T}^E]\!] = \varepsilon_e \left\{ \frac{1}{2}\left[E_n^2 \left(1 - \frac{\sigma_r^2}{\varepsilon_r}\right) - E_t^2 \right] \boldsymbol{n} + E_n E_t \left(1 - \frac{\sigma_r}{\varepsilon_r}\right) \boldsymbol{t} \right\}. \tag{6}$$

The electric field $\boldsymbol{E} = -\nabla\phi$, where ϕ is the electric potential that satisfies the Laplace equation both inside and outside the drop in the extended leaky dielectric model

$$\nabla^2 \phi_j = 0. \tag{7}$$

Far away from the drop surface the electric field is the imposed electric field

$$-\nabla \phi_e = E_0 \boldsymbol{z}. \tag{8}$$

At the drop surface the tangential electric field is continuous while the normal electric field has a jump due to the displacement current:

$$[\![\nabla\phi \cdot \boldsymbol{t}]\!] = 0, \quad [\![\sigma \nabla\phi \cdot \boldsymbol{n}]\!] = \frac{\partial q}{\partial t}, \tag{9}$$

where $q \equiv [\![-\varepsilon \nabla\phi \cdot \boldsymbol{n}]\!]$ is the surface charge density with σ the conductivity of the fluid. While charge relaxation ($\partial q/\partial t$) may be significant for large drops (such as mm-sized Tween-laden drops in silicone oil), here we assume that charge relaxation is negligible ($\partial q/\partial t \approx 0$) for smaller drops as a first approximation. In this case, the conservation of current Eq. (9) reduces to the continuity of Ohmic current, $[\![\sigma \nabla\phi \cdot \boldsymbol{n}]\!] = 0$.

The surfactant transport on the drop surface in the Lagrangian framework is described by the following equation:

$$\frac{\partial \Gamma}{\partial t} + \nabla_s \cdot (\boldsymbol{u}_s \Gamma) + \kappa \boldsymbol{u} \cdot \boldsymbol{n} \Gamma = D_s \nabla_s^2 \Gamma, \tag{10}$$

where Γ is the surfactant concentration, $\nabla_s \equiv (\mathbf{I} - \boldsymbol{n}\boldsymbol{n}) \cdot \nabla$ is the gradient projected on the drop surface, $\boldsymbol{u}_s \equiv (\mathbf{I} - \boldsymbol{n}\boldsymbol{n}) \cdot \boldsymbol{u}$ is the tangential velocity on the surface, κ is the mean curvature, and D_s is the diffusion constant of the surfactant on the drop surface.

1. Analytical solution

The spheroidal coordinates system has been used successfully to analyze the electrohydrodynamics of clean [11,33,34] and surfactant-laden [32] leaky dielectric drops. The large deformation analysis, to contrast with the oft-used small-deformation theory, rests on assumptions that naturally constrain its validity. We expand on these limitations in Appendix B 1. However, we note that in the case of surfactant-laden drops, provided the drop remains spheroidal, our model agrees well with experimental and numerical data for moderate and large Péclet numbers [35]. Here we only provide a general outline of the method used to derive the shape equation Sec. II A 2. Focusing on the axisymmetric flow, the prolate spheroidal coordinates (ξ, η) can be expressed in the cylindrical coordinates (r, z) as

$$z = c\xi\eta, \quad r = c\sqrt{(\xi^2 - 1)(1 - \eta^2)}, \tag{11}$$

where $c \equiv \sqrt{a^2 - b^2}$ is the semifocal length, and a and b are the major and minor semiaxis, respectively. Defined as such, $\xi \in [1, \infty)$, $\eta \in [-1, 1]$, and surfaces of constant ξ are spheroids while surfaces of constant η are hyperboloids. Therefore, the prolate drop surface is simply given by $\xi = \xi_0(t) \equiv a/c$. Volume conservation of the drop relates a and b to $\xi_0(t)$ as $a(t) = r_0/\sqrt[3]{1 - \xi_0(t)^{-2}}$ and $b(t) = r_0\sqrt[6]{1 - \xi_0(t)^{-2}}$. In the following we use h_ξ, h_η, and h_ζ to denote the metric coefficients in the prolate spheroidal coordinates. The hydrodynamic and electric potential problems can be solved separately. The potential ϕ is obtained by solving Eq. (7) for both ϕ_i and ϕ_e with boundary and matching conditions at the drop surface [34]:

$$\phi_e = [-E_0 c\xi + \alpha(t) Q_1(\xi)]\eta, \tag{12}$$

$$\phi_i = \beta(t)\xi\eta, \tag{13}$$

with

$$\alpha(t) = \frac{\xi_0 \beta(t) + E_0 c \xi_0}{Q_1(\xi_0)}, \tag{14}$$

and $Q_1(\xi)$ the first-degree Legendre polynomial of the second kind. In the absence of charge relaxation, the boundary condition in the normal direction given by Eq. (9) reduces to the widely used interfacial boundary condition

$$[\![\sigma \nabla\phi]\!] = \sigma_e \frac{\partial \phi_e}{\partial \xi} - \sigma_i \frac{\partial \phi_i}{\partial \xi} = 0 \text{ at } \xi = \xi_0. \tag{15}$$

With this simplified interfacial condition, the electric potential coefficients $\alpha(t)$, $\beta(t)$ are given by

$$\alpha(t) = \frac{c\xi_0(\sigma_r - 1)}{\xi_0\sigma_r Q_1' - Q_1}, \quad \beta(t) = \frac{c\sigma_r(Q_1 - \xi_0 Q_1')}{\xi_0\sigma_r Q_1' - Q_1}, \tag{16}$$

where the primes denote derivatives with respect to ξ.

Next we focus on the hydrodynamic problem. The axisymmetric two-dimensional incompressible fluid velocity is related to a stream function ψ both inside and outside the drop via

$$u_j = -\frac{1}{h_\xi h_\zeta}\frac{\partial \psi_j}{\partial \xi}, \quad v_j = \frac{1}{h_\eta h_\zeta}\frac{\partial \psi_j}{\partial \eta}, \tag{17}$$

where u and v are the tangential and normal components (relative to the drop surface) of the fluid velocity. The stream function satisfies the equation

$$(\nabla^2)^2\psi = 0, \tag{18}$$

with

$$\nabla^2 = \frac{1}{c^2(\xi^2 - \eta^2)}\left[\frac{\partial}{\partial \xi}(\xi^2 - 1)\frac{\partial}{\partial \xi} + \frac{\partial}{\partial \eta}(1 - \eta^2)\frac{\partial}{\partial \eta}\right].$$

The general solution to Eq. (18) can be expressed using the method of semidecomposition,

$$\psi = g_0(\xi)G_0(\eta) + g_1(\xi)G_1(\eta) + \sum_{n=2}^{\infty} g_n(\xi)G_n(\eta) + h_n(\xi)H_n(\eta), \tag{19}$$

where G_n and H_n are Gegenbauer functions of the first and second kinds, respectively. g_n and h_n are linear combinations of G_n and H_n. Interested readers are referred to Dassios *et al.* [36] for detailed expressions of G_n, H_n, g_n and h_n. Following the approaches in Bentenitis and Krause [11] and Zhang et al. [34], we seek an approximate solution

$$\psi_e = \left[A_3^1 H_1(\xi) + A_3^3 H_3(\xi)\right]G_3(\eta), \tag{20}$$

$$\psi_i = \left[B_3^3 G_3(\xi) + B_3^5 G_5(\xi)\right]G_3(\eta). \tag{21}$$

The tangential velocity is continuous across the drop surface and has to be determined consistently through the stress balance, while the normal component of the interface velocity can be computed explicitly as

$$v(\xi_0) = \frac{r_0(1 - \xi_0^{-2})^{-5/6}}{3\xi_0^2}\frac{(1 - 3\eta^2)}{\sqrt{\xi_0^2 - \eta^2}}\frac{d\xi_0}{dt}.$$

The coefficients A_3^1, B_3^3, and B_3^5 are determined from the continuity of velocities at the drop surface together with the kinematic condition $\boldsymbol{u}\cdot\boldsymbol{n} = v(\xi_0)$. The remaining coefficient A_3^3 and the rate of deformation of drop shape $d\xi_0/dt$ are computed from the stress balance equation [Eq. (6)] averaged over the drop surface in the energetic fashion as done by Zhang *et al.* [34]. In spheroidal coordinates, the tangential and normal components of the averaged stress, respectively, are

$$\int_{\xi=\xi_0(t)} u\left[\left[\!\left[T_{\xi\eta}^H\right]\!\right] + \left[\!\left[T_{\xi\eta}^E\right]\!\right] + \frac{1}{h_\eta}\frac{\partial \gamma}{\partial \eta}\right]ds = 0, \tag{22}$$

$$\int_{\xi=\xi_0(t)} v\left[\left[\!\left[T_{\xi\xi}^H\right]\!\right] + \left[\!\left[T_{\xi\xi}^E\right]\!\right] - \gamma(\nabla\cdot\boldsymbol{n})\right]ds = 0. \tag{23}$$

It is straightforward to show $A_3^1 = A_3^3 H_3 - M d\xi_0/dt$, $B_3^3 = (-A_3^3 G_5 H_3' + M G_5' d\xi_0/dt)/N$, and $B_3^5 = (A_3^3 G_3 H_3' - M G_3' d\xi_0/dt)/N$, where $M = 2c^3/3$ and $N = G_3 G_5' - G_5 G_3'$. At steady state ($d\xi_0/dt = 0$), all coefficients in Eqs. (20) and (21) can be expressed in terms of A_3^3, which therefore represents the strength of the flow field inside and outside the drop.

2. Shape equation

We nondimensionalize lengths using the drop radius r_0, and time using the EHD flow timescale $\tau_{\mathrm{EHD}} = r_0/U$, where U is a characteristic velocity. The electric potential is scaled using $E_0 r_0$, and surface tension using γ^* of the convection-free case. In terms of the variables we have $\alpha = E_0 r_0 \tilde{\alpha}$, $\beta = E_0 r_0 \tilde{\beta}$, and $c = r_0\tilde{c}$. Hereafter, we drop the tildes for simplicity and refer to only dimensionless quantities unless otherwise stated.

The coefficient A_3^3 is determined from the stress balance as

$$A_3^3 = \frac{-\mathrm{Ca}_E c^3 \mathcal{Q}_T \xi_0 f_{11} + \mathcal{E} c^2 f_{17} - \mathrm{Ca}_E[(\mu_r - 1)f_{12} + f_{13}]M\dfrac{d\xi_0}{dt}}{-(\mu_r f_{14} + f_{15})}, \tag{24}$$

where $\mathrm{Ca}_E = E_0^2 r_0 \varepsilon_e/\gamma^*$ is the electric capillary number, $\mathcal{E} = E\chi/[1 + E\ln(1 - \chi)]$, and the elasticity number $E = RT\Gamma_\infty/\gamma_0$ is a measure of the sensitivity of surface tension to changes in the concentration of adsorbed surfactant on the drop surface, expressed in terms of the gas constant R, temperature T and the surface tension of a clean drop γ_0. The system is closed with the evolution equation for the prolate drop shape ξ_0,

$$\frac{d\xi_0}{dt} = \frac{3}{2}\frac{f_{\mathcal{Q}_N} + f_{\mathcal{Q}_T} + f_{\mathrm{Ma}} + f_\gamma}{(\mu_r f_{25} + f_{26})}, \tag{25}$$

where

$$f_{\mathcal{Q}_N} = \mathcal{Q}_N f_{21}, \tag{26a}$$

$$f_{\mathcal{Q}_T} = \mathcal{Q}_T\frac{\xi_0 f_{11}(\mu_r f_{22} + f_{23})}{\mu_r f_{14} + f_{15}}, \tag{26b}$$

$$f_{\mathrm{Ma}} = -\frac{E\chi}{\mathrm{Ca}_E c[1 + E\ln(1 - \chi)]}\frac{f_{17}(\mu_r f_{22} + f_{23})}{\mu_r f_{14} + f_{15}}, \tag{26c}$$

$$f_\gamma = -\frac{f_{24}}{\mathrm{Ca}_E}, \tag{26d}$$

$$\mathcal{Q}_N = \frac{1}{c^2}\left\{[-c+\alpha(t)Q_1']^2 + \left[-c+\alpha(t)\frac{Q_1}{\xi_0}\right]^2 - 2\frac{\beta^2(t)}{\varepsilon_r}\right\}, \tag{26e}$$

$$\mathcal{Q}_T = \frac{1}{c^2}\left\{[-c+\alpha(t)Q_1'][-c+\alpha(t)\frac{Q_1}{\xi_0}] - \frac{\beta^2(t)}{\varepsilon_r}\right\}. \tag{26f}$$

$f_{\mathcal{Q}_N}$, $f_{\mathcal{Q}_T}$, f_{Ma}, and f_γ represent, respectively, the contributions of the Maxwell stresses, Marangoni stress and surface tension to the shape of the drop. The shape-dependent functions f_{11}, f_{12}, f_{13}, f_{14}, f_{15}, f_{17}, f_{21}, f_{22}, f_{23}, f_{24}, f_{25}, and f_{26} are provided in Appendix A. In the absence of charge relaxation, contributions from the Maxwell stresses $f_{\mathcal{Q}_N}$ given by Eq. (26a) and $f_{\mathcal{Q}_T}$ given by Eq. (26b) reduce to

$$f_{\mathcal{Q}_N} = -K^2\left(2\frac{\sigma_r^2}{\varepsilon_r} - \sigma_r^2 - 1\right)f_{21},$$
$$f_{\mathcal{Q}_T} = K^2\sigma_r\left(1-\frac{\sigma_r}{\varepsilon_r}\right)\frac{\xi_0 f_{11}(\mu_r f_{22}+f_{23})}{\mu_r f_{14}+f_{15}}, \tag{27}$$

where $K \equiv [Q_1(\xi_0) - \xi_0 Q_1'(\xi_0)]/[Q_1(\xi_0) - \sigma_r \xi_0 Q_1'(\xi_0)]$.

B. Conducting drops

For a conducting drop the conductivity ratio $\sigma_r \ll 1$, and consequently there is no tangential electric field on the interface ($E_t = \boldsymbol{E}\cdot\boldsymbol{t} \to 0$) [33,37,38]. The general formulation for the bulk follows that of leaky dielectric drops: The fluids in the exterior and interior are governed by the incompressible Stokes Eqs. (1) and (2) with prescribed far-field and kinematic boundary conditions. The main difference is in the boundary conditions that are related to the Maxwell stress $\mathbf{T}^E$: For a conducting drop, Eq. (6) reduces to

$$[\![\mathbf{T}^E]\!] = \frac{\varepsilon_e}{2}E_n^2\boldsymbol{n}. \tag{28}$$

In terms of spheroidal coordinates for a conducting drop, Eq. (22) reduces to

$$\int_{\xi=\xi_0(t)} u\left([\![T^H_{\xi\eta}]\!] + \frac{1}{h_\eta}\frac{\partial\gamma}{\partial\eta}\right)ds = 0. \tag{29}$$

In the absence of tangential electric stresses, Eq. (29) informs us that the hydrodynamic flow is instead balanced by Marangoni stresses. In this case the velocity U scales as γ^*/μ_e, giving $t = \tau_\gamma \tilde{t}$ where $\tau_\gamma = r_0\mu_e\gamma^*$ is the hydrodynamic timescale. We obtain the flow strength

$$A_3^3 = \frac{\mathcal{E}c^2 f_{17} - [(\mu_r-1)f_{12}+f_{13}]M\dfrac{d\xi_0}{dt}}{-(\mu_r f_{14}+f_{15})}, \tag{30}$$

and the shape equation

$$\frac{d\xi_0}{dt} = \frac{3}{2}\frac{f_{\mathcal{Q}_N}+f_{\mathrm{Ma}}+f_\gamma}{(\mu_r f_{25}+f_{26})}, \tag{31}$$

where $f_{\mathcal{Q}_T} = 0$ and $f_{\mathcal{Q}_N}$ now takes the form

$$f_{\mathcal{Q}_N} = \frac{\mathrm{Ca}_E}{c^2}\left[(-c+\alpha(t)Q_1')^2 - 2\frac{\beta^2(t)}{\varepsilon_r}\right]f_{21}. \tag{32}$$

C. Surface tension and surfactant transport

We adopt the Langmuir equation of state for the surface tension γ of the surfactant-laden drop surface

$$\gamma = \gamma_0[1 + E\ln(1-\Gamma)]. \tag{33}$$

The Langmuir equation of state is not valid for surfactant concentration above the maximum packing concentration, beyond which the integrity of the surfactant monolayer is compromised by micelle formation. This is often observed during tip streaming [39–41] and thread formation [42,43]. Here, we only consider equilibrium drop shape for low to moderate surfactant concentration, below the maximum packing concentration.

The equation for the surfactant concentration is nondimensionalized by scaling the surfactant by $\Gamma = \Gamma^*\tilde{\Gamma}$, where Γ^* is the surfactant distribution in the convection-free case ($D_s \to \infty$), and the surface tension $\gamma = \gamma^*\tilde{\gamma}$, where $\gamma^* = \gamma_0[1 + E\ln(1-\chi)]$. Again dropping the tildes, the equation of state becomes

$$\gamma(\Gamma) = \frac{1 + E\ln(1-\chi\Gamma)}{1+E\ln(1-\chi)}, \tag{34}$$

where $\chi = \Gamma^*/\Gamma_\infty$ is the surfactant coverage.

The dimensionless surfactant transport equation

$$\mathrm{Pe}_s\left[\frac{\partial\Gamma}{\partial t} + \nabla_s\cdot(\Gamma\boldsymbol{u}_s) + (\boldsymbol{u}\cdot\boldsymbol{n})\kappa\Gamma\right] = \nabla_s^2\Gamma, \tag{35}$$

where $\mathrm{Pe}_s = Ur_0/D_s$ is the dimensionless Péclet number (a measure of the relative importance of convective transport to diffusive transport), and U is a characteristic velocity.

For electrically driven flow U scales as $\varepsilon_e E_0^2 r_0/\mu$, and the Péclet number is proportional to the square of the electric field strength. We can then estimate the Péclet number by considering typical values for a Tween-laden drop in silicone oil. The oil phase has viscosity $\mu \approx 10$ Pa s and dielectric constant $\varepsilon_e/\varepsilon_0 = 2.2 - 2.9$, where ε_0 is the vacuum permittivity [44]. In experiments [2,44–46], typical values of the electric field are in the order of kV/cm. For a drop of size one millimeter [45], the velocity U is estimated of order 10^{-3} mm/s. With surfactant diffusivity $D_s \approx 10^{-10}$ m^2/s [47], we obtain Péclet number of order 10. For smaller drops with size of order tens of microns [2,46], the Péclet number could be as small as 10^{-3}. Thus, we can expect diffusive transport to contribute significantly to the dynamics.

In the axisymmetric spheroidal coordinates, Eq. (35) takes the following form:

$$\mathrm{Pe}_s\left[\frac{\partial\Gamma}{\partial t} + \frac{u}{h_\eta}\frac{\partial\Gamma}{\partial\eta} + \left(\frac{1}{h_\eta}\frac{\partial u}{\partial\eta} + \kappa v\right)\Gamma\right] = \frac{1}{h_\eta}\frac{\partial}{\partial\eta}\left(\frac{1}{h_\eta}\frac{\partial\Gamma}{\partial\eta}\right). \tag{36}$$

The large deformation spheroidal analysis provides an efficient tool to determine the drop shape and the corresponding flow field compared to direct numerical simulations of the full system. The nonlinear surfactant transport equation [Eq. (36)], however, may not be tractable analytically except for some asymptotic limits in Péclet number. To investigate the dynamics for a range of intermediate Péclet number, we develop a hybrid, semianalytical approach to solve the full set of equations. The spheroidal representation of the

drop shape is combined with a numerical collocation method for determining the surfactant concentration profile on the spheroidal surface. Details of the numerical implementation can be found in Appendix B 2.

III. MODEL VALIDATION

Conducting drops can only achieve prolate shapes at equilibrium due to the absence of electric field-induced tangential flows. Since our main focus is to contrast the effects of surfactant transport on leaky dielectric versus conducting drops, extension to oblate shapes is beyond the scope of this paper and is deferred to future studies. Furthermore, we consider identical viscosity between the continuous phase and the drop ($\mu_r = 1$), and the surfactant elasticity $E = 0.2$. We characterize drop deformation via the deformation number $D \equiv (a-b)/(a+b)$.

A. Equilibrium deformation of clean conducting drops

The large deformation analysis of a viscous drop has garnered increasing interest in recent years. In the absence of surfactants [the surface tension γ is a constant and $f_{\mathrm{Ma}} = 0$ in Eq. (31)], large-deformation studies have shown excellent agreements with both numerical simulations [10] and experiments [6] for a leaky dielectric drop under a DC electric field. The main reason for the growing popularity of the large-deformation analysis is that without too much more work than the small-deformation analysis, the spheroidal model for a clean drop in a DC field gives excellent agreement with experimental data over a wide range of capillary number and deformation as long as the drop shape remains spheroidal (see the Appendix in Ref. [32]).

Here we show the accuracy of the large-deformation analysis for the case of clean spheroidal conducting drops. At the steady equilibrium $d\xi_0/dt = 0$ in Eq. (31), giving $\mathcal{Q}_N f_{21} = f_{24}$, where $\mathcal{Q}_N$ is given by Eq. (26e). This equation is nonlinear in the drop shape coordinate ξ_0. Alternatively, we can consider the inverse problem of determining the electric capillary number Ca_E for a given drop shape ξ_0. Figure 2 shows the comparison between the results obtained from solving for ξ_0 from Eq. (31) and numerical simulations [48] and experiments (triangle and circle symbols) [6,48] of electrohydrodynamics of a conducting drop. We also plot results for the first- [3] and second-order [49] small-deformation theory. At small values of the electric capillary number ($\mathrm{Ca}_E \leqslant 0.1$) all analytical and numerical models are in excellent agreement with the experimental data. The first-order small deformation approximation underestimates the equilibrium drop deformation around $\mathrm{Ca}_E \approx 0.1$, while predictions from the second-order small deformation model hold up to $\mathrm{Ca}_E \approx 0.15$. For this problem, the spheroidal model captures the full range of experimental observations as well as numerical simulations.

B. Effects of surfactant coverage on drops deformation

In this section, and in the rest of the analysis, we focus our attention on two distinct modes of deformation: prolate "A" drop that exhibits counter-clockwise (equator to pole) circulation; and prolate "B" drop with clockwise circulation (pole to equator). For comparison we use the same values

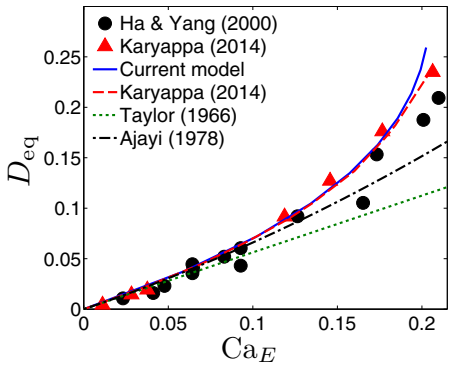

FIG. 2. Equilibrium deformation D_{eq} as a function of electric capillary number for a clean conducting drop. The parameters $\mu_r = 1/0.00126$, $\sigma_r = 10^{-8}$, $\varepsilon_r = 1/31.1$. The symbols denote experiments [6,48]; the curves represent predictions using the boundary integral method (dashed) [48], Taylor's first-order theory (dotted), and Ajayi's second-order approximation (dash-dotted). The present model is shown in solid line.

for the dimensionless parameters as in [31]: $\varepsilon_r = 1$, $\sigma_r = 1/3$ for prolate "A," and $\varepsilon_r = 1/3.5$, $\sigma_r = 1/3$ for prolate "B." In particular, these two cases have been found to demonstrate very interesting dynamics in direct numerical simulations [31]: For a prolate "A" drop with $(\varepsilon_r, \sigma_r) = (1, 1/3)$ addition of surfactant produces larger deformation than the clean drop case. Moreover, increasing surfactant coverage yields more pronounced drop deformation.

For small to moderate surfactant coverage, previous direct numerical simulations with finite Péclet number ($\mathrm{Pe}_s = 10$) [31] and spheroidal model with nondiffusive surfactant ($\mathrm{Pe}_s \to \infty$) [32] showed that increasing surfactant coverage gives rise to larger drop deformation regardless of electric field strength. This phenomenon is related to tip-stretching (for a detailed explanation, see Ref. [32]), where the average surface tension is small and surfactant concentration gradient (and hence Marangoni stress) is large.

In contrast, for high surfactant coverage, the equilibrium drop deformation depends on the electric field strength [39]: the deformation, larger at low to moderate values of electric field strength compared to the clean drop case, is subsequently suppressed as the electric capillary number increases. This phenomenon is known as surface dilution. In this paper we focus on surfactant coverages $\chi \leqslant 0.5$ and on the range of electric capillary number Ca_E where tip-stretching is expected to dominate.

Figure 3(a) illustrates the excellent agreement in equilibrium deformation between the current model (solid curves), numerical simulations using regularized method (diamonds), [31] and boundary integral simulations (circles) [35]. Figure 3(b) shows the comparison between our model and numerical simulations for the prolate "B" drop. While our predictions agree very well with boundary integral simulations, we observe some discrepancies with results from Ref. [31] as Ca_E increases. These discrepancies may be attributed to the weak inertial effect in the regularized level-set method [31], which is absent in the results by the boundary integral method and the current semianalytical model. We note that, for prolate "A" drops, the fluid stress combines with the

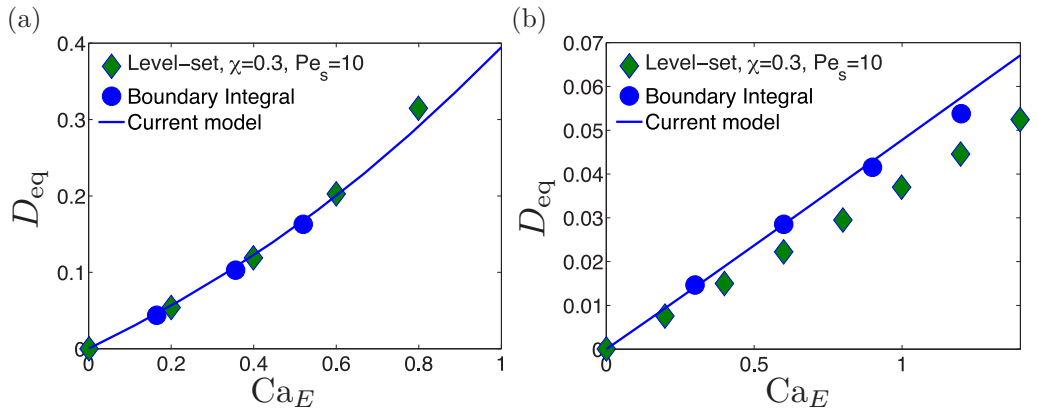

FIG. 3. Equilibrium deformation $D_{\rm eq}$ as a function of electric capillary number for a surfactant-laden, leaky dielectric drop. The electric parameters are (a) for a prolate "A" (counterclockwise circulation) drop with $\varepsilon_r = 1,\ \sigma_r = 1/3$; and (b) for a prolate "B" (clockwise) drop with $\varepsilon_r = 1/3.5,\ \sigma_r = 1/3$. Symbols are from numerical simulations using a regularized level-set method [31] (green diamond), and a boundary integral equation method (blue circle) [35]; the current semianalytical approach is represented by the solid line.

electric stress to deform a drop along the direction of the electric field, while the opposite holds for prolate "B" drops. We thus speculate that inertial effects (which influences the fluid stress [50,51]) may cause the discrepancies observed in Fig. 3(b). Nevertheless, the overall relative errors between the boundary integral simulations and the current model are less than 10% in all cases studied.

IV. EFFECTS OF SURFACTANT TRANSPORT ON EQUILIBRIUM DEFORMATION

In this section we perform a systematic investigation of the effect of Pe_s on equilibrium drop deformation $D_{\rm eq}$, exploring how surfactant transport and coverage combine to affect equilibrium drop shapes under a dc electric field.

A. Leaky dielectric drops

Figure 4 shows equilibrium drop deformation $D_{\rm eq}$ in Fig. 4(a) and flow strength A_3^3 in Fig. 4(b) for a prolate "A" leaky dielectric drop with $\mathrm{Ca}_E = 0.67$. Figure 4(c) shows the Marangoni stress and surface tension (inset) at different values of χ for $\mathrm{Pe}_s = 0.1$. For small Pe_s (diffusion dominated regime) the equilibrium drop deformation $D_{\rm eq}$ decreases with surfactant coverage χ while A_3^3 increases with χ. The corresponding dependencies of the Marangoni stress and surface tension are consistent with such a trend: As χ increases, both surface tension and Marangoni stress increase in magnitude, consistent with the decreasing trend of $D_{\rm eq}$ and the increasing trend of A_3^3. Our simulation results show that such trend in $D_{\rm eq}$ is reversed for $\mathrm{Pe}_s \geqslant 6$: $D_{\rm eq}$ increases with χ while A_3^3 still increases with χ. The dependence of equilibrium drop deformation on the surface Péclet number is also observed for a viscous drop under an external flow [52].

For $\mathrm{Pe}_s \gg 6$, convection dominates; surfactant is swept, and accumulates, near the pole where it reduces the surface tension locally. In this process, known as tip stretching, the electric, hydrodynamic, and Marangoni forces combine to deform the drop in the direction of the electric field. The deformation is consistent with previous works and experiments:

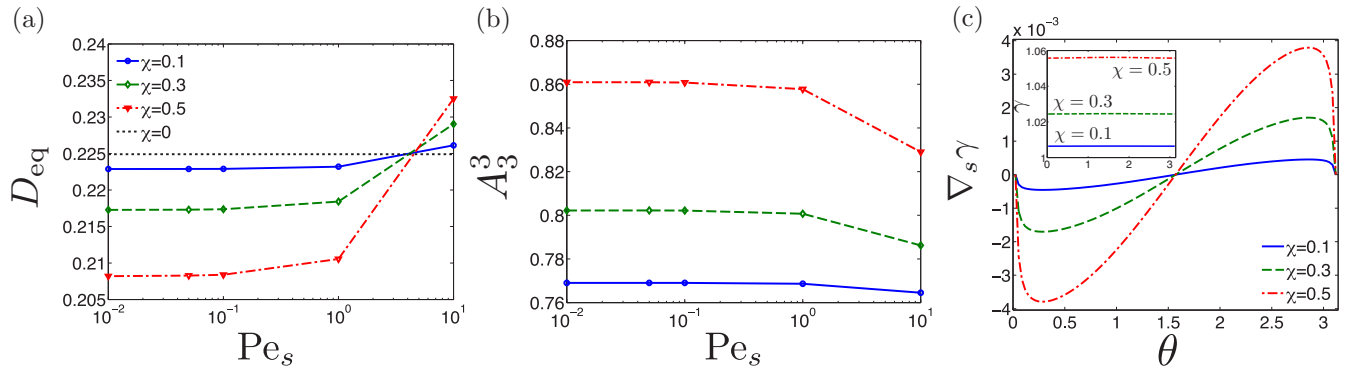

FIG. 4. Effects of Péclet number on the deformation number ($D_{\rm eq}$) and flow strength (A_3^3) for a leaky dielectric prolate "A" drop with $\varepsilon_r = 1,\ \sigma_r = 1/3$. In (a) $D_{\rm eq}$ shows dependence on both surfactant coverage and Pe_s. For $\mathrm{Pe}_s \lesssim 5$, $D_{\rm eq}$ decreases with increasing χ; above that threshold, the opposite holds: $D_{\rm eq}$ increases with higher surfactant coverage. No such transition is observed in A_3^3. In (b), A_3^3 monotonically decreases with increasing Pe_s, and higher surfactant coverage yields stronger flow. In (c) the Marangoni stress ($\nabla_s\gamma$) and surface tension (γ, in inset) are plotted as a function of $\theta = \cos^{-1}(\eta)$ for $\mathrm{Pe}_s = 0.1$. The electric capillary number $\mathrm{Ca}_E = 0.67$

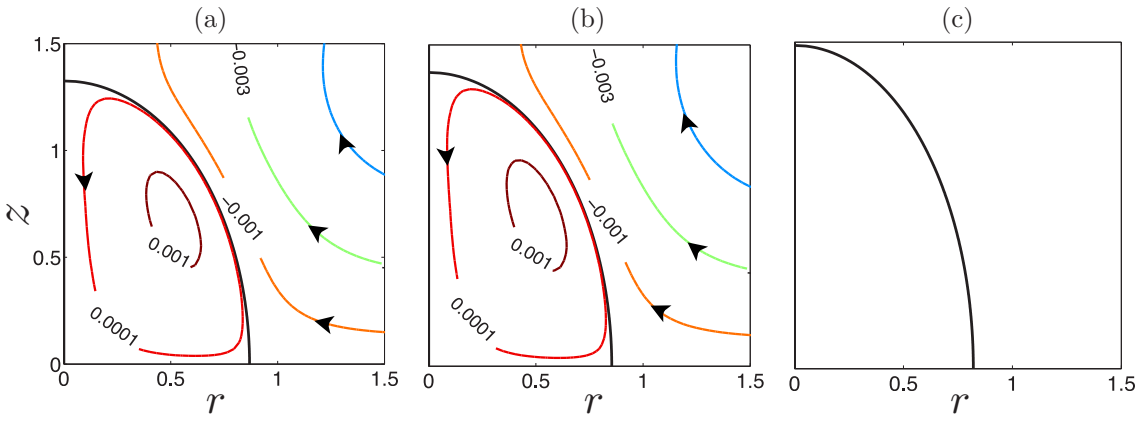

FIG. 5. Streamlines for the leaky dielectric prolate "A" drop with $\varepsilon_r = 1$, $\sigma_r = 1/3$, and $\chi = 0.5$: (a) $\mathrm{Pe}_s = 0.01$; (b) $\mathrm{Pe}_s = 10$; and (c) $\mathrm{Pe}_s \to \infty$ (the nondiffusive case from [32]). As the Péclet number Pe_s increases from (a) to (c), we observe larger deformation. In the nondiffusive limit the flow is completely suppressed as shown in (c).

It increases with χ, and the larger degree of deformation is accompanied with stronger convective transport. For large but finite Péclet numbers A_3^3 decreases with increasing Pe_s but is not completely suppressed, unlike the case of nondiffusive surfactants ($\mathrm{Pe}_s \to \infty$) where the drop surface is completely immobilized by surfactants and the flow strength $A_3^3 \to 0$ [32].

Surfactants have a twofold effect on drop electrohydrodynamics. On one end, for a given transport regime (fixed Pe_s), the velocity field around a surfactant-covered drop is greatly reduced by surfactant coverage [31,32]. On the other end, surfactant transport also affects drop electrohydrodynamics. In Fig. 5, we plot the streamlines for various values of Péclet number: $\mathrm{Pe}_s = 0.01$ [Fig. 5(a)], $\mathrm{Pe}_s = 10$ [Fig. 5(b)], and the nondiffusive case in Ref. [32] [$\mathrm{Pe}_s \to \infty$, Fig. 5(c)]. As Pe_s increases from Figs. 5(a) to 5(c), we observe increasing deformation and decreasing flow strength [consistent with A_3^3 in Fig. 4(b)]. Figures 6(a) and 6(b) show the equilibrium deformation D_{eq} and flow strength A_3^3 for a leaky dielectric prolate "B" drop with $\mathrm{Ca}_E = 1.4$. For this prolate shape, increasing the surfactant coverage leads to equilibrium drop deformation smaller than a clean drop [31,32] as captured by our model in Fig. 6(a) for $\mathrm{Pe}_s \gtrapprox 0.1$. For such a prolate "B" drop the surfactant is swept from the pole to the equator, yielding smaller surface tension at the equator than at the poles. Thus, the deformation along the direction of the electric field (prolate "A") is suppressed and the equilibrium drop shape is nearly spherical.

For diffusion-dominant surfactant transport ($\mathrm{Pe}_s < 0.1$), D_{eq} is nearly independent of surfactant coverage χ. However, closer inspection (see insets in Fig. 6) reveals that higher surfactant coverage yields larger deformation. Dominated by diffusion, surfactants distribute evenly over the surface of the drop. Electric stresses that drive prolate "A" shape result in slightly larger surfactant concentration near the poles, where the reduction in surface tension leads to higher deformation number. In this case, the smaller change in deformation number compared to the prolate "A" case is ascribed to the clockwise circulation opposing deformation along the direction of the electric field.

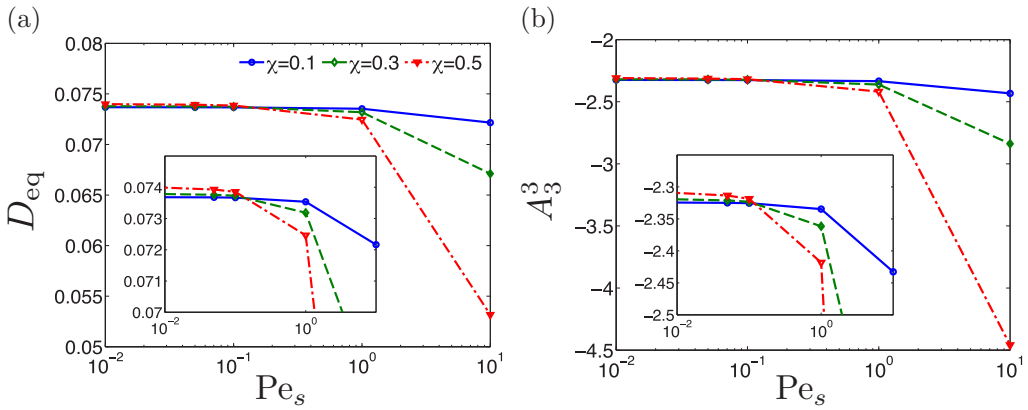

FIG. 6. Effects of Péclet number on the deformation number (D_{eq}) and flow strength (A_3^3) for a leaky dielectric prolate "B" drop with $\varepsilon_r = 1/3.5$, $\sigma_r = 1/3$. The transition from diffusion- to convection-dominated dynamics occurs around $\mathrm{Pe}_s \approx 10^{-1}$. In the diffusion-dominated regime, higher surfactant coverage yields larger deformation (and stronger flow), though the difference between these is minimal. In the convection-dominated regime, we observe that D_{eq} decreases with Pe_s while the magnitude of flow strength ($|A_3^3|$) increases with Pe_s. The electric capillary number $\mathrm{Ca}_E = 1.4$.

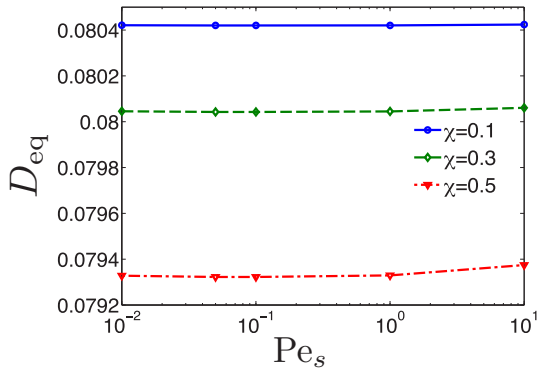

FIG. 7. Equilibrium deformation number as a function of Péclet number for a conducting drop. The effects of surfactant transport is shown for various values of surfactant coverage at $Ca_E = 0.112$. The electric parameters are $\sigma_r = 10^{-3}$, $\varepsilon_r = 1$.

The flow strength, represented by A_3^3 in Fig. 6(b), varies with Pe_s in a similar fashion as drop deformation. Slightly stronger flow correlates with higher surfactant coverage for $Pe_s < 0.1$, and weaker flow dominates with lower surfactant concentration for $Pe_s \gtrapprox 0.1$. Furthermore, the large magnitudes in Fig. 6(b) relative to Fig. 4(b) are consistent with stronger hydrodynamic stresses that are necessary to resist deformation along the direction of the electric field.

B. Conducting drops

At steady equilibrium $\partial\Gamma/\partial t = 0$ and $\boldsymbol{u}\cdot\boldsymbol{n} = 0$, thus we deduce from the surfactant transport equation [Eq. (10)] that $\boldsymbol{u}_s\Gamma \propto \nabla_s\Gamma$. In the surfactant diffusion dominant regime, the surfactant distribution is rendered nearly uniform by strong diffusion, and thus $\nabla_s\Gamma \approx 0$ and the tangential hydrodynamic stress also has to vanish at steady equilibrium. In the case of a conducting drop, there is no tangential Maxwell stress and therefore the flow strength (A_3^3) depends only the average surfactant concentration gradient [f_{17} in Eq. (30)]. Thus, we conclude that on a conducting drop, both the tangential velocity ($\boldsymbol{u}_s \approx 0$) and the Marangoni stress ($\nabla_s\gamma \approx 0$) vanish in the diffusion-dominant regime of surfactant transport. This implies that the conducting drop covered with surfactant is immobilized when the surfactant diffusion is strong. Moreover, we expect the equilibrium deformation to be dependent on surfactant coverage and insensitive to Péclet number in the diffusion-dominant regime.

We consider the case of a prolate drop with $\sigma_r = 10^{-3}$ and $\varepsilon_r = 1$. In Fig. 7, we plot the deformation number as a function of the Péclet. The result shows that surfactant transport does not seem to affect the dynamics of a conducting drop, and the deformation number is essentially independent of Pe_s. Moreover, increasing the surfactant coverage χ yields smaller deformation, although the change in deformation from $\chi = 0.1$ to $\chi = 0.5$ is less than 2%. The inverse relation between surfactant coverage and drop deformation suggests the surface dilution dominates the surfactant dynamic for a conducting drop over a wide range of Péclet numbers. We also note that unlike leaky dielectric drops, there is no distinction between prolate "A" and "B" shapes, since tangential electric stresses are nonexistent.

V. EFFECTS OF SURFACTANT TRANSPORT ON TRANSIENT DYNAMIC

Studies of drops in electric field, and unsteady flow field ($\partial\boldsymbol{u}/\partial t$) [8,21] or surface charge relaxation $\partial q/\partial t$ [21] revealed nonmonotonic time evolution of the deformation. Time-dependent flow produces an overshoot in the unsteady deformation of the drop prior to reaching equilibrium, while $\partial q/\partial t$, characterized by the Saville number $\mathcal{S}a$ [21], displays a shape transition at the early stage of transient deformation.

In the case of surfactant, the unsteady transport equation [Eq. (35)] shows that the influence of $\partial\Gamma/\partial t$ and $\nabla_s\cdot(\Gamma\boldsymbol{u}_s)$ grows significantly with Pe_s. While the effects of surfactant convection on the equilibrium electrodeformation have been investigated [31,32], changes in drop dynamics due to unsteady surfactant transport ($\partial\Gamma/\partial t$) remain to be determined. Figure 8(a) shows the transient deformation of a leaky

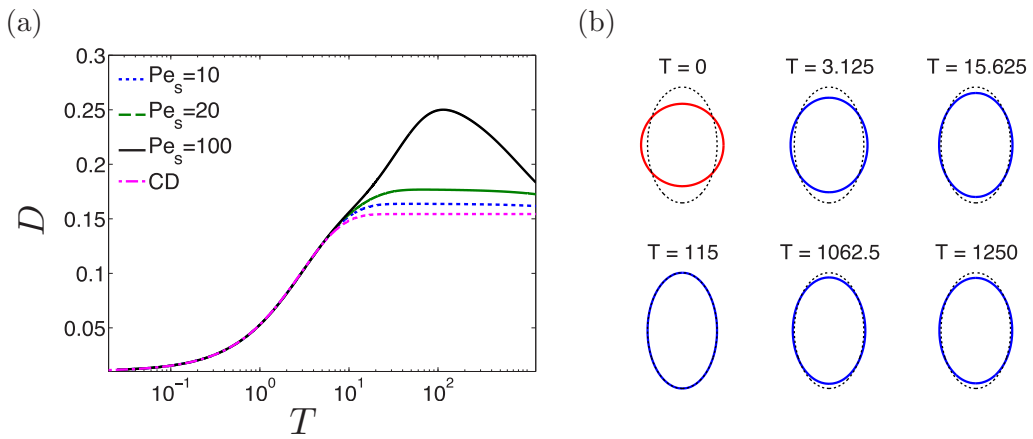

FIG. 8. (a) Deformation number D as a function of dimensionless time for a leaky dielectric drop with various values of Pe_s. The electric capillary number $Ca_E = 0.5$ and surfactant coverage $\chi = 0.3$; the electric parameters $\varepsilon_r = 1$, $\sigma_r = 1/3$, corresponding to the prolate "A" shape. The steady-state curve for the clean drop case (CD) is denoted by the dotted line. (b) Snapshot of the drop shape at various times for D in (a) with $Pe_s = 100$. The dashed shape denotes the maximum shape achieved at peak overshoot.

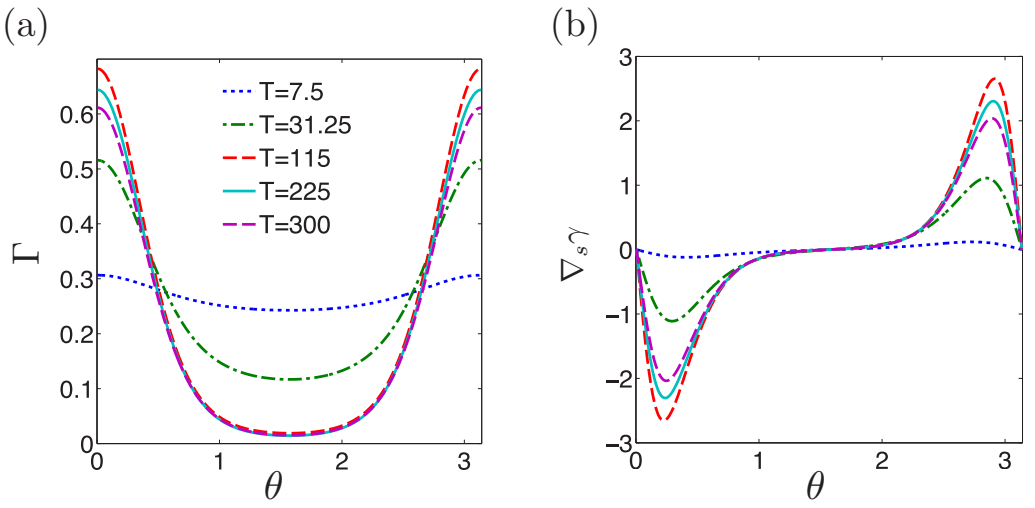

FIG. 9. The surfactant profile (a) and Marangoni stress (b) corresponding to $\mathrm{Pe}_s = 100$ in Fig. 8 are plotted as a function of $\theta = \cos^{-1}(\eta)$. Each curve denotes a fixed time, with the peak overshoot occurring at $T \approx 115$.

dielectric prolate "A" drop under an electric field. We vary $\mathrm{Pe}_s \in [10, 20, 100]$ with $\mathrm{Ca}_E = 0.5$ and $\chi = 0.3$. As expected from Sec. IV, the equilibrium deformation number depends on the surface Péclet number: Stronger surfactant transport leads to larger deformation number. Furthermore, for these parameters, all curves display a transient overshoot, although negligible for $\mathrm{Pe}_s \leqslant 1$. The feature becomes more pronounced for $\mathrm{Pe}_s > 1$: It reaches around 1% of the equilibrium shape when $\mathrm{Pe}_s = 10$ and around 36% when $\mathrm{Pe}_s = 100$. In Fig. 8(b) we show snapshots of the drop shape at various times with $\mathrm{Pe}_s = 100$. The dashed curve denotes the maximum deformed shape achieved by the drop, at the peak of the overshoot. The maximum shape is reached around $T \approx 115$. From that point, the drop shape settles to its equilibrium.

Figure 9 shows the corresponding distributions of surfactant concentration [Fig. 9(a)] and Marangoni stress [Fig. 9(b)] as a function of the surface parameter $\theta = \arccos(\eta)$ at various time instances. Transient overshoots of surfactant concentration and Marangoni stress near the poles are observed at $T \approx 115$. However, the causal relationship of these correlations with the transient overshoot in deformation is not obvious and will be investigated in the future; here we only report these correlations.

The deformation of a leaky dielectric drop under an electric field is the result of induced (creeping) flow caused by tangential Maxwell stresses. However, these tangential stresses do not exist in perfectly conducting drops. We ran simulations for the perfectly conducting drop (keeping all parameters unchanged from the prolate "A" case in Fig. 8) and observed only monotonic behaviors of the unsteady deformation, suggesting the importance of tangential flows in leaky dielectric drops and the transient overshoot due to surfactant.

VI. CONCLUSION

We investigate the effect of surfactant transport on the electrodeformation of a viscous drop under a DC electric field. Extending previous work on nondiffusive surfactant [32] here we focus on two surfactant transport regimes characterized by the surface Péclet number (Pe_s). The advantage of our modal approach over direct numerical simulations is that we can identify salient features of surfactant-laden drop electrodynamics by efficiently examining the deformation dynamics for different combinations of parameter values. We derived analytical equations describing the electrodeformation of surfactant-laden leaky dielectric and conducting drops (both clean and surfactant-laden) in the presence of insoluble surfactants. We validate our model by comparing against published results from both experiments and numerical simulations, and found good agreement for the clean conducting drops [6,48], and the surfactant-laden drops [31]. We then perform a systematic study of the effects of surfactant transport on the equilibrium drop deformation.

In this study we focus on two modes of prolate deformation: one with counterclockwise circulation ("A") and another with clockwise circulation ("B"). Depending on the surfactant transport regime, we observe different behaviors of deformation for leaky dielectric drops: when surfactant diffusion dominates ($\mathrm{Pe}_s \ll 1$), prolate "A" ("B") yields smaller (larger) equilibrium deformation with increasing surfactant coverage, compared to a clean drop. However, when convection dominates ($\mathrm{Pe}_s \gg 1$), the equilibrium drop deformation increases (decreases) with larger surfactant coverage on a prolate "A" ("B") drop. We also contrast leaky dielectric versus conducting drops in Appendix C. For a prolate "A" drop we find consistently larger equilibrium drop deformation for a leaky dielectric drop compared to a conducting drop, while for prolate 'B' we identify cases where larger deformation is found for a conducting drop compared to a leaky dielectric drop. Finally, we study the effect of the surfactant transport on the evolution of drop shape. We found the drop undergoes an overshoot in the early deformation phase, before settling to its equilibrium shape—a dynamic similar to the overshoot observed for electrohydrodynamic governed by the unsteady Stokes equation [21].

Another important aspect of surfactant-laden drop electrohydrodynamics is surfactant solubility, known to lead to drastically different drop dynamics in the absence of an

external electric field [43]. Recent experiments with soluble surfactants have revealed rich dynamics of drops electrohydrodynamics under a strong electric field [53]. Future theoretical investigations will attempt to provide insights into how surfactant solubility and electrohydrodynamics may combine to affect the drop deformation and dynamics. Specifically, we ponder whether the flow is still suppressed when sorption kinetics are accounted for, or if surfactant solubility can be used to control the electrodeformation of drops, and/or alter the dynamics in the various transport regimes. We are now expanding our model to incorporate the exchange of surfactant between the drop surface and the bulk under an electric field.

Finally, we remark that charge relaxation, which is not accounted for in this work, may become important for systems with small drops or large interfacial surface. It has been shown recently that finite charge relaxation can lead to interesting dynamics for clean drops [21]. Its influences on the transient behavior of surfactant-laden drops may be more prominent when the drop is undergoing extreme deformation such as breakup.

ACKNOWLEDGMENTS

H.N. thanks K. Pietrzyk for helpful discussions about the analytical derivations and C. Sorgentone for providing boundary integral simulation results for comparison. Y.-N.Y. was partially supported by NSF under Grants No. DMS-1412789 and No. DMS-1614863 and by the Flatiron Institute, a division of the Simons Foundation. O.S.P. was partially supported by NSF under Grant No. EFMA-1830958.

APPENDIX A: INTEGRALS IN THE PROLATE SPHEROIDAL MODEL

The functions $f_{11}(\xi_0)$–$f_{15}(\xi_0)$ in Eq. (25) are given by

$$f_{11} = \int \frac{\eta G_3(\eta)}{\xi_0^2 - \eta^2} d\eta, \tag{A1}$$

$$f_{12} = \frac{1}{\xi_0^2 - 1} \int G_3(\eta) \left[\frac{2\eta G_3'(\eta)}{(\xi_0^2 - \eta^2)^2} + \frac{G_3''(\eta)}{\xi_0^2 - \eta^2} \right] d\eta, \tag{A2}$$

$$f_{13} = \frac{G_3' G_5'' - G_5' G_3''}{2N} f_{11}, \tag{A3}$$

$$f_{14} = -\xi_0 H_3' \int \frac{\eta G_3(\eta)}{(\xi_0^2 - \eta^2)^2} d\eta + \frac{H_3''}{2} f_{11}, \tag{A4}$$

$$f_{15} = \xi_0 H_3' \int \frac{\eta G_3(\eta)}{(\xi_0^2 - \eta^2)^2} d\eta - \frac{(G_3 G_5'' - G_5 G_3'') H_3'}{2N} f_{11}, \tag{A5}$$

$$f_{17} = \frac{1}{\sqrt{\xi_0^2 - 1}} \int_{-1}^{1} \frac{G_3(\eta)\Gamma'(\eta)}{\sqrt{\xi_0^2 - \eta^2}(1 - \chi\Gamma)} d\eta. \tag{A6}$$

Furthermore, the functions $f_{21}(\xi_0)$–$f_{26}(\xi_0)$ in Eqs. (25) and (31) are given by

$$f_{21} = \frac{\xi_0^2}{2} \int \frac{(3\eta^2 - 1)(\eta^2 - 1)}{\xi_0^2 - \eta^2} d\eta, \tag{A7}$$

$$f_{22} = -H_3' \int \frac{(1 - 3\eta^2)(2\eta^4 + \xi_0^2 - 3\xi_0^2\eta^2)}{(\xi_0^2 - \eta^2)^2} d\eta + 3H_3\xi_0 \int \frac{1 - 3\eta^2}{\xi_0^2 - \eta^2} d\eta, \tag{A8}$$

$$f_{23} = -\frac{49}{30N} G_3 H_3' (1 - 3\xi_0^2) + H_3' \int \frac{(1 - 3\eta^2)(2\eta^4 + \xi_0^2 - 3\xi_0^2\eta^2)}{(\xi_0^2 - \eta^2)^2} d\eta, \tag{A9}$$

$$f_{24} = \frac{1}{c} \left[\xi_0 (\xi_0^2 - 1)^{1/2} \int \frac{\gamma(3\eta^2 - 1)}{(\xi_0^2 - \eta^2)^{3/2}} d\eta + \frac{\xi_0}{(\xi_0^2 - 1)^{1/2}} \int \frac{\gamma(3\eta^2 - 1)}{(\xi_0^2 - \eta^2)^{1/2}} d\eta \right], \tag{A10}$$

$$f_{25} = -\frac{\xi_0}{\xi_0^2 - 1} \int \frac{(1 - 3\eta^2)(2\xi_0^2 - \eta^2 - 1) G_3'(\eta)}{(\xi_0^2 - \eta^2)^2} d\eta + 3\xi_0 \int \frac{1 - 3\eta^2}{\xi_0^2 - \eta^2} d\eta - \frac{(\mu_r - 1) f_{12} + f_{13}}{\mu_r f_{14} + f_{15}} f_{22}, \tag{A11}$$

$$f_{26} = \frac{\xi_0}{\xi_0^2 - 1} \int \frac{(1 - 3\eta^2)(2\xi_0^2 - \eta^2 - 1) G_3'(\eta)}{(\xi_0^2 - \eta^2)^2} d\eta - \frac{49}{30N} (1 - 3\xi_0^2) G_3' - \frac{(\mu_r - 1) f_{12} + f_{13}}{\mu_r f_{14} + f_{15}} f_{23}. \tag{A12}$$

γ is the dimensionless surface tension given by Eq. (34), and $N = G_3 G_5' - G_5 G_3'$.

APPENDIX B: NUMERICAL ALGORITHM DETAILS

1. Model limitations

We made some assumptions to arrive at the shape Eqs. (25) and (31). Here we discuss how these assumptions affect predictions using our model. First, based on experimental findings, we assume the drop remains spheroidal in shape. However, other subtle shape variations may be at play during the drop dynamics, and these may account for discrepancies in the electrodeformation at moderate to high values of electric

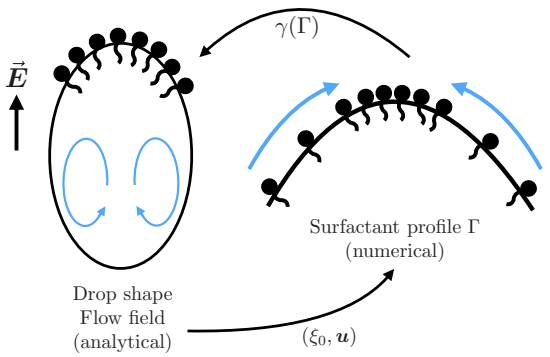

FIG. 10. The semianalytical algorithm: At t_n the drop shape ξ_0 and flow field $\boldsymbol{u}$ is computed using the large deformation spheroidal analysis. This information is then used as input to the surfactant transport, to determine the surfactant profile Γ numerically with a collocation method. With the surfactant concentration at hand, we determine the change in surface tension, the drop shape and the flow field at time t_{n+1}. This process is repeated until a steady state is reached.

capillary number. Second, only the first spheroidal harmonics mode is considered in this study. The truncation error, coupled with averaging the stress balances, influences the flow circulation and, by extension, surfactant dynamics.

Moreover, for a surfactant-covered drop, once the surfactant concentration reaches the maximum packing at a location on the drop surface, the fluid flow and the interface deformation there conspire to immobilize the drop surface so that no more surfactant can flux into that location [39,54–56]. Such suppression of interfacial flow can only be approximated in our modal analysis with a single mode.

2. Numerical implementation

The steps we take to simulate the dynamic of a surfactant-laden drop in an electric field are illustrated in Fig. 10. At time t_n, the governing equation for the drop shape ξ_0 and the surfactant transport equation are solved numerically using various algorithms. The integrals involving the Marangoni stress (f_{17}) and the surface tension (f_{24}) are resolved by Gauss-Legendre quadrature with n nodes that are used to discretize the drop spatial distribution η. We then use the integrals to solve the ordinary differential Eqs. (25) and (31) using a fourth-order Runge-Kutta method. Once the drop shape, and consequently the flow field, are obtained, the information is used to obtain the surfactant distribution profile. The surfactant concentration Γ is obtained by solving the transport equation [Eq. (36)]. This is a nonlinear equation that does not admit analytical solutions, except in special limits [32,57]. To consider the full range of Péclet number, we treat the surfactant transport as a boundary value problem and solve the equation using MATLAB's built-in *bvp4c* function, a finite difference code that implements the three-stage Lobatto Illa collocation method [58]. The boundary value problem is set up as a system of two ordinary differential equations with variables $y_1 = \Gamma$ for the surfactant concentration and $y_2 = d\Gamma/d\eta$. Surfactant conservation is enforced by augmenting the system $\{y_1, y_2\}$ with a third variable $y_3 \equiv \int_{-1}^{\eta} \Gamma h_\eta h_\zeta d\eta$, with boundary condition $y_3(1) =$ total amount of surfactant. Once the surfactant concentration Γ is obtained, we determine the change in the surface tension γ, and feed the result back into Eqs. (25) and (31) to determine the drop shapes and flow fields at the next time step t_{n+1}. This process is repeated until either a steady state is reached, when the change in successive ξ_0 iterates $|\Delta\xi_0| \leqslant 10^{-6}$, or the simulation stops, signaling that a spheroidal shape is not attainable.

APPENDIX C: COMPARISON BETWEEN LEAKY DIELECTRIC AND CONDUCTING DROPS

To facilitate comparison with the leaky dielectric drop in the previous section, we now consider the leaky drop with $\sigma_r = 1/3$. We note this is strictly for comparison purpose since for a conducting drop it is necessary $\sigma_r \ll 1$. However, we point out that even in this case, the dependence of the deformation number on surfactant transport and surfactant coverage is qualitatively the same. Figure 11(a) shows the deformation number for a prolate "A" conducting drop with $\mathrm{Ca}_E = 0.67$, while Fig. 11(b) shows the deformation number for a prolate "B" conducting drop with $\mathrm{Ca}_E = 1.4$. Here as

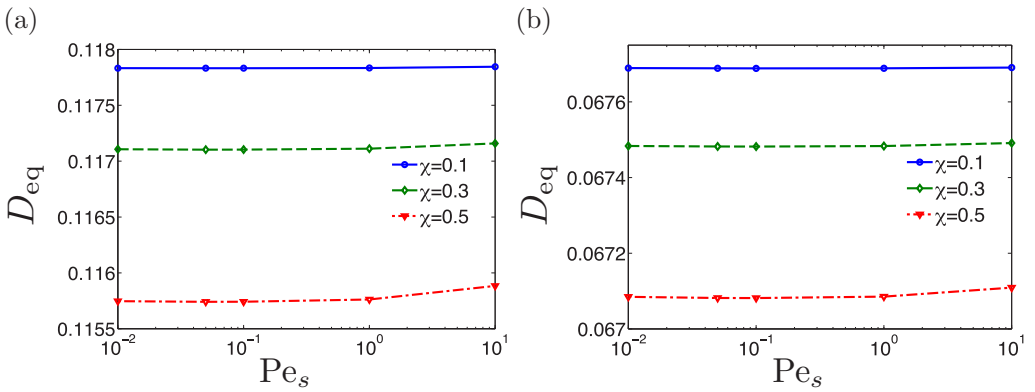

FIG. 11. Effects of Péclet number on the deformation number (D_{eq}) for (a) a conducting prolate "A" drop with $\varepsilon_r = 1$, $\sigma_r = 1/3$ and $\mathrm{Ca}_E = 0.67$, and (b) a conducting prolate "B" drop with $\varepsilon_r = 1/3.5$, $\sigma_r = 1/3$ and $\mathrm{Ca}_E = 1.4$. In both cases the deformation remains relatively constant across $\mathrm{Pe}_s \lessapprox 1$, then shows small increases as convection starts dominating. Moreover, higher surfactant coverage yields smaller deformation.

well, as shown in Fig. 11(a), deformation remains independent of Pe_s. Also, the change in deformation between $\chi = 0.1$ and $\chi = 0.5$ is less than 2%.

The importance of electric tangential stresses and the induced flow in surfactant transport is evident when we contrast the flow strength A_3^3 for leaky dielectric drops (of order 10^{-1} [Fig. 4(b)]), to a vanishingly small flow strength A_3^3 in conducting drops. The deformation in Fig. 11(b) for a prolate "B" drop is also independent of Pe_s, with an increase in the surfactant coverage yielding a negligible enhancement in deformation. We attribute the similarities between Figs. 11(a) and 11(b) to the lack of tangential flows in a conducting viscous drop.

When contrasting leaky dielectric and conducting drops, both laden with insoluble surfactant with $\mathrm{Pe}_s \gg 1$, we generally expect a leaky dielectric drop would undergo larger deformation than a conducting drop [see Fig. 6(a) versus Fig. 11(b)]. This is because the additional tangential flows in leaky dielectric drops contribute significantly to overall deformation. However, we found that when conditions are such that moderate surfactant concentration is combined with strong convection and clockwise flow circulation, conducting drops can actually yield larger deformation than a leaky dielectric drop at equilibrium. Closer analysis of Figs. 6(a) and 11(b) reveals that for $\mathrm{Pe}_s = 10$, $D_{\mathrm{eq}} = 0.0532$ for a leaky dielectric drop, while $D_{\mathrm{eq}} = 0.0671$ for a conducting drop, or 26% larger. Note that while the change in deformation is significant, it may prove difficult to observe in experiments since D_{eq} is of order 10^{-2}. For experimental validation, it is more helpful to compare the flow field via A_3^3 with clear variations in order of magnitude. Indeed, for a prolate "B" leaky dielectric drop $A_3^3 \approx -4.5$ [Fig. 6(b)] compared to a vanishingly small A_3^3 for a conducting drop.

[1] C. T. O'Konski and H. C. Thacher, J. Chem. Phys. **57**, 955 (1953).
[2] R. S. Allan and S. G. Mason, Proc. R. Soc. Lond. A **267**, 45 (1962).
[3] G. Taylor, Proc. R. Soc. Lond. A **291**, 159 (1966).
[4] J. R. Melcher and G. I. Taylor, Annu. Rev. Fluid Mech. **1**, 111 (1969).
[5] D. A. Saville, Annu. Rev. Fluid Mech. **29**, 27 (1997).
[6] J.-W. Ha and S.-M. Yang, J. Fluid Mech. **405**, 131 (2000).
[7] E. K. Zholkovskij, J. H. Masliyah, and J. Czarnecki, J. Fluid Mech. **472**, 1 (2002).
[8] G. Supeene, C. R. Koch, and S. Bhattacharjee, J. Colloid Int. Sci. **318**, 463 (2008).
[9] J.-W. Ha and S.-M. Yang, Phys. Fluids **12**, 764 (2000).
[10] E. Lac and G. M. Homsy, J. Fluid Mech. **590**, 239 (2007).
[11] N. Bentenitis and S. Krause, Langmuir **21**, 6194 (2005).
[12] M. Zabarankin, SIAM J. Appl. Math. **73**, 677 (2013).
[13] M. Zabarankin, SIAM J. Appl. Math. **76**, 1606 (2016).
[14] P. R. Brazier-Smith, Phys. Fluids **14**, 1 (1971).
[15] P. R. Brazier-Smith, S. G. Jennings, and J. Latham, Proc. R. Soc. Lond. A **325**, 363 (1971).
[16] M. Miksis, Phys. Fluids **24**, 1967 (1981).
[17] O. A. Basaran and L. E. Scriven, Phys. Fluids **1**, 799 (1989).
[18] H. Nganguia, Y.-N. Young, A. T. Layton, W.-F. Hu, and M.-C. Lai, Commun. Comput. Phys. **18**, 429 (2015).
[19] W.-F. Hu, M.-C. Lai, and Y.-N. Young, J. Comp. Phys. **282**, 47 (2014).
[20] G. I. Taylor, in *Proceedings of the Eleventh International Congress of Applied Mechanics (Munich 1964)* (Springer Verlag, Heidelberg, 1964), pp. 790–796.
[21] J. A. Lanauze, L. M. Walker, and A. S. Khair, Phys. Fluids **25**, 112101 (2013).
[22] J. A. Lanauze, L. M. Walker, and A. S. Khair, J. Fluid Mech. **774**, 245 (2015).
[23] D. Das and D. Saintillan, J. Fluid Mech. **810**, 225 (2017).
[24] J. Q. Feng, Proc. R. Soc. Lond. A **455**, 2245 (1999).
[25] H. Nganguia, Y.-N. Young, A. T. Layton, M.-C. Lai, and W.-F. Hu, Phys. Rev. E **93**, 053114 (2016).
[26] H. A. Stone and L. G. Leal, J. Fluid Mech. **220**, 161 (1990).
[27] P. M. Vlahovska, Phys. Rev. Fluids **1**, 060504 (2016).
[28] S. Takagi and Y. Matsumoto, Annu. Rev. Fluid Mech. **43**, 615 (2011).
[29] J.-W. Ha and S.-M. Yang, J. Colloid Int. Sci. **175**, 369 (1995).
[30] J.-W. Ha and S.-M. Yang, J. Colloid Int. Sci. **206**, 195 (1998).
[31] K. E. Teigen and S. T. Munkejord, Phys. Fluids **22**, 112104 (2010).
[32] H. Nganguia, Y.-N. Young, P. M. Vlahovska, J. Bławzdziewcz, J. Zhang, and H. Lin, Phys. Fluids **25**, 092106 (2013).
[33] N. Dubash and A. J. Mertel, J. Fluid Mech. **581**, 469 (2007).
[34] J. Zhang, J. D. Zahn, and H. Lin, Phys. Rev. E **87**, 043008 (2013).
[35] C. Sorgentone, A.-K. Tornberg, and P. Vlahovska, J. Comput. Phys. **389**, 111 (2019).
[36] G. Dassios, M. Hadjinicolaou, F. A. Coutelieris, and A. C. Payatakes, Int. J. Engng Sci. **33**, 1465 (1995).
[37] N. Dubash and A. J. Mertel, Phys. Fluids **19**, 072101 (2007).
[38] N. Dubash and A. J. Mertel, Phys. Fluids **19**, 073104 (2007).
[39] Y. Pawar and K. J. Stebe, Phys. Fluids **8**, 1738 (1996).
[40] C. D. Eggleton, T.-M. Tsai, and K. J. Stebe, Phys. Rev. Lett. **87**, 048302 (2001).
[41] M. R. Booty and M. Siegel, J. Fluid Mech. **544**, 243 (2005).
[42] M. Hameed, M. Siegel, Y.-N. Young, J. Li, M. R. Booty, and D. T. Papageorgiou, J. Fluid Mech. **594**, 307 (2008).
[43] Y.-N. Young, M. R. Booty, M. Siegel, and J. Li, Phys. Fluids **21**, 072105 (2009).
[44] P. F. Salipante and P. M. Vlahovska, Phys. Fluids **22**, 112110 (2010).
[45] M. Ouriemi and P. M. Vlahovska, J. Fluid Mech. **751**, 106 (2014).
[46] V. Vivacqua, S. Mhatre, M. Ghadiri, A. M. Abdullah, A. Hassanpour, M. J. Al-Marri, B. Azzopardi, B. Hewakandamby, and B. Kermani, Chem. Eng. Res. Des. **104**, 658 (2015).
[47] A. Balakrishnan, B. D. Rege, G. L. Amidon, and J. E. Polli, J. Pharm. Sci. **93**, 2064 (2004).
[48] R. B. Karyappa, S. D. Deshmukh, and R. M. Thaokar, J. Fluid Mech. **754**, 550 (2014).
[49] O. O. Ajayi, Proc. R. Soc. Lond. A **364**, 499 (1978).
[50] L. G. Leal, Ann. Rev. Fluid Mech. **12**, 435 (1980).

[51] Y. Y. Renardy and V. Cristini, Phys. Fluids **13**, 7 (2001).
[52] W. J. Milliken, H. A. Stone, and L. G. Leal, Phys. Fluids **5**, 69 (1993).
[53] J. A. Lanauze, R. Sengupta, B. J. Bleier, B. A. Yezer, A. S. Khair, and L. M. Walker, Soft Matter **14**, 9351 (2018).
[54] C. D. Eggleton, Y. P. Pawar, and K. J. Stebe, J. Fluid Mech. **385**, 79 (1999).
[55] C. D. Eggleton and K. J. Stebe, J. Coll. Int. Sci. **208**, 68 (1998).
[56] Y. Wang, D. Papageorgiou, and C. Maldarelli, J. Fluid Mech. **390**, 251 (1999).
[57] C. Kallendorf, A. Fath, M. Oberlack, and Y. Wang, Phys. Fluids **27**, 082104 (2015).
[58] *MATLAB version 8.3.0.532 (R2014a)* (The Mathworks, Natick, MA, 2014).